Journal of Alloys and Compounds 903 (2022) 163948

Contents lists available at ScienceDirect

Journal of Alloys and Compounds

journal homepage: www.elsevier.com/locate/jalcom

Revealing the ductile-to-brittle transition mechanism in polycrystalline body-centered tetragonal tin (Sn) for cryogenic electronics

Xiaoliang Ji[a,b,1], Rong An[c,1,*], Wei Zhou[a], Ying Zhong[d], Fu Guo[a], Chunqing Wang[b,*]

[a] Faculty of materials and manufacturing, Beijing University of Technology, Beijing 100124, China
[b] State Key Laboratory of Advanced Welding and Joining, Harbin Institute of Technology, Harbin 150080, China
[c] Key Laboratory of Micro-systems and Micro-structures Manufacturing of Ministry of Education, Harbin Institute of Technology, Harbin 150080, China
[d] Department of Mechanical Engineering, University of South Florida, Tampa, FL 33620, USA

ARTICLE INFO

Article history:
Received 6 December 2021
Received in revised form 18 January 2022
Accepted 22 January 2022
Available online 26 January 2022

Keywords:
Ductile-to-brittle transition
Polycrystalline Sn
Deformation twinning
Dislocation glide
Cryogenic electronics

ABSTRACT

The inherent ductile-to-brittle transition (DBT) of body-centered tetragonal Sn at cryogenic temperatures restricts the use of Sn-based solders in the interconnection of cryogenic electronics, but little is known about the deformation behaviors accompanying with the transition and the underlying transition mechanism. In this work, the deformation features before cryogenic brittle fracture and the DBT mechanism in polycrystalline Sn were studied through uniaxial tensile experiments at different temperatures. Compared to the softening process stimulated by dynamic recovery and dynamic recrystallization before ductile fracture at room temperature (~293 K), a high strain hardening rate (~5% of the shear modulus) is maintained during the linear hardening period preceding brittle fracture at the liquid nitrogen temperature (~77 K) due to the pronounced intersecting of {301} deformation twins. But the irreconcilable velocity difference between dislocation glide (~3 μm/s) and twin thickening (~10 μm/s) at 77 K leads to a premature brittle fracture in the midst of the linear hardening, and indeed the DBT. The suggested specific DBT mechanism is substantiated by the fact that a significant increase in the velocity (~1500 μm/s) with the increasing temperature (123 K) allows the dislocation slip to readily accommodate the shear strains due to {301} twin thickening at the grain boundaries, thereby resulting in ductile fracture rather than brittle fracture. This deep understanding about the DBT in polycrystalline Sn may help forge a new path to design ductile and strong Sn-based solders and solder joints for cryogenic electronics by deformation twinning.
© 2022 Elsevier B.V. All rights reserved.

1. Introduction

Tin (Sn), as the matrix of most solder alloys, is indispensable in modern electronic manufacturing. Sn-based solders provide the electrical and mechanical connections between the chip and the pad as well as between the component (encapsulated chip) and the printed circuit board (PCB) [1,2]. Because the joined components are usually much stiffer, the high stress induced either thermally or mechanically is imparted primarily to these soft Sn–based solders [3]. By virtue of excellent ductility of Sn matrix, the Sn-based solders can absorb the high thermal or mechanical stress. However, a ductile-to-brittle transition (DBT) would take place in the Sn matrix when the ambient temperature decreases below a critical temperature [4–7]. The DBT of Sn matrix would lead to abrupt fracture of solder bulk under stress at cryogenic temperatures [4]. This transition is therefore a potential devastating hazard to those cold survivable and cold operational electronics, such as electrical instruments servicing in Antarctic expedition (213 K) [8] and extraterrestrial space (Mars:133 K, Moon: 93 K) [9], high sensitivity photonic detectors (77 K) [10], and bioelectronics (77 K or lower) [11,12]. Moreover, since the low-temperature allotropic transformation of Sn (βSn→αSn) requires nucleation and growth with an incubation period of days [13] and even months [14], the DBT behavior corresponds exactly to the βSn with the body-centered tetragonal (BCT) structure [7].

Sn single crystal, as a model system, has been chosen to investigate the brittle fracture mechanism at cryogenic temperatures [7,15]. It has been found that deformation twinning occurs as a dominant deformation mechanism in the Sn single crystal and thus should be responsible for the DBT. But it is generally accepted that twins can permit a large plastic deformation rather than lead to

* Corresponding authors.
E-mail addresses: anr@hit.edu.cn (R. An), wangcq@hit.edu.cn (C. Wang).
[1] These authors contributed equally to this work

https://doi.org/10.1016/j.jallcom.2022.163948
0925-8388/© 2022 Elsevier B.V. All rights reserved.

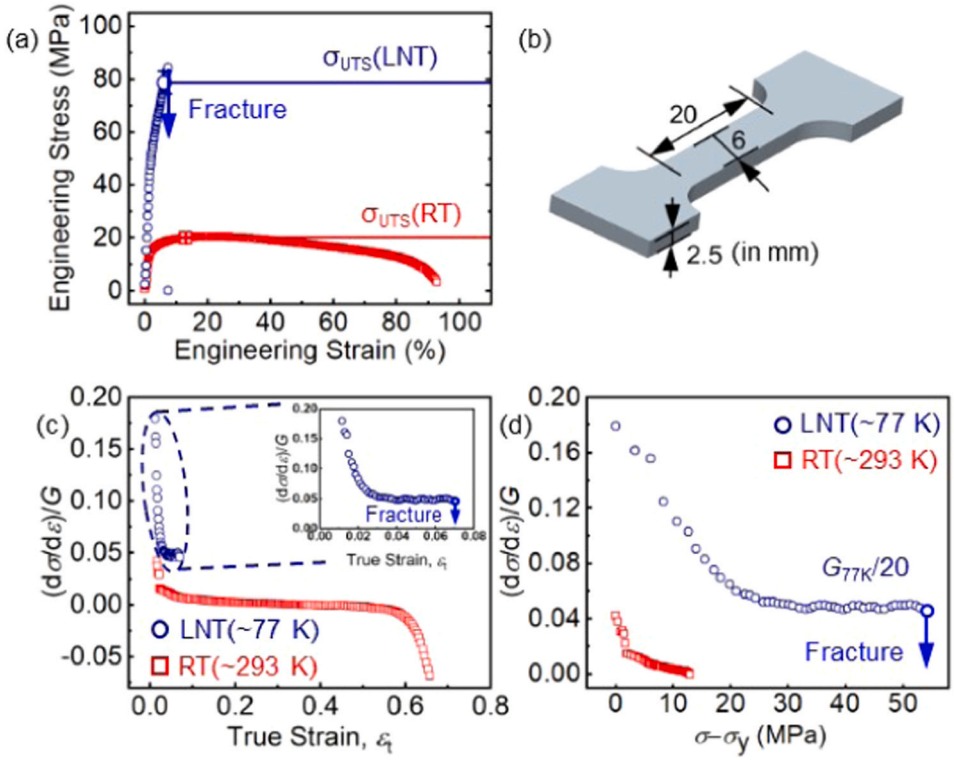

Fig. 1. (a) Engineering stress-strain curves of polycrystalline Sn specimens at LNT (~77 K, blue circles) and RT (~293 K, red squares). (b) Geometry dimensions of the tensile samples. Normalized true strain hardening rates by shear modulus, $(d\sigma/d\varepsilon)/G$ are plotted as a function of (c) true strain and (d) flow stress, σ-σ_y. Inset in (b): the details of hardening rate-strain curve at LNT.

brittleness [16–18]. On the other hand, the polycrystalline form of Sn is exactly encountered in the engineering solder alloys [19,20] while the DBT behavior of polycrystalline Sn is more complicated and affected by many factors such as grain boundary (GB). Therefore, it is challenging but significant to understand the mechanism of DBT occurring in polycrystalline Sn. Previous investigations on the DBT of polycrystalline Sn focus on the determination of the ductile-to-brittle transition temperature (DBTT) [4,5,21] and influence factors on the DBTT including cooling rate [22] and alloying elements [4,21,23] by the Charpy impact test. However, due to the transient characteristic of the Charpy impact test [24], the mechanism of DBT has not been well connected with the deformation process before brittle fracture and thus remains unclear.

In this paper, we carried out uniaxial tensile experiments with a high strain rate of 0.01/s on polycrystalline Sn to investigate the cryogenic deformation behaviors before brittle fracture and further reveal the DBT mechanism. Electron backscattered diffraction (EBSD), transmission electron microscopy (TEM) and fractography characterizations and pertinent theoretical calculations demonstrate consistently that the plastic deformation of polycrystalline Sn before cryogenic brittle fracture is dominated by deformation twinning; while the decreasing velocity of dislocation glide with temperature cannot keep up with the twin growth rate in *thickness*, causing the cryogenic brittle failure. The precise mechanism can be useful in designing Sn-based solders and solder joints with improved mechanical performance and embrittlement resistance for cryogenic electronics.

2. Experimental methods

2.1. Materials and mechanical testing

The materials investigated in this work are commercially pure cast polycrystalline Sn (> 99.99% pure) with a BCT crystal structure (I4/mmm). The rectangular dog-bone shaped tensile specimens with a gauge length of 20 mm were machined from the cast slabs by wire electrical discharge machining. Both sides of these specimens were ground using SiC paper into a final thickness of ~2.5 mm. The geometry dimensions of the tensile samples are illustrated in Fig. 1b.

Considering that the DBT commonly occurs in deformation conditions at high strain rates but the transient Charpy impact test cannot reveal the accompanying deformation features with DBT, uniaxial tensile tests were conducted at a high engineering strain rate of 0.01/s in an Instron 5500 R load frame. Sets of four samples were tested at each temperature including room temperature (RT, ~293 K) and the liquid nitrogen temperature (LNT, ~77 K). Each tensile specimen was immersed in the cryogenic environment for 30 min preceding tensile experiments.

2.2. Microstructure characterizations

The microstructures were analyzed using an EBSD technique on the surface of tensile specimens deformed at different temperatures. In all the EBSD scans, the transverse direction (TD) of the sample stage was set parallel to the tensile axis (TA). Specimens were electro-polished in a mixture of perchloric acid and acetic with 1:9 in volume ratio for EBSD characterizations under scanning electron microscope (SEM, FEI, Quanta 200 FEG). The electron beam energy was set to 30 kV and the scanning step size was 1 μm. EBSD data were collected and analyzed using TSL OIM data collection 6 and OIM analysis 6, respectively. These EBSD data were used for orientation mapping, misorientation distribution analysis and twin characterizations. Moreover, because the EBSD characterizations were done at RT for the specimens fractured at LNT, we evaluated the effect of temperatures on the microstructures and confirmed that the original microstructural features of the LNT tensile specimens were still retained in the RT-EBSD analysis (See Supplementary Material 1).

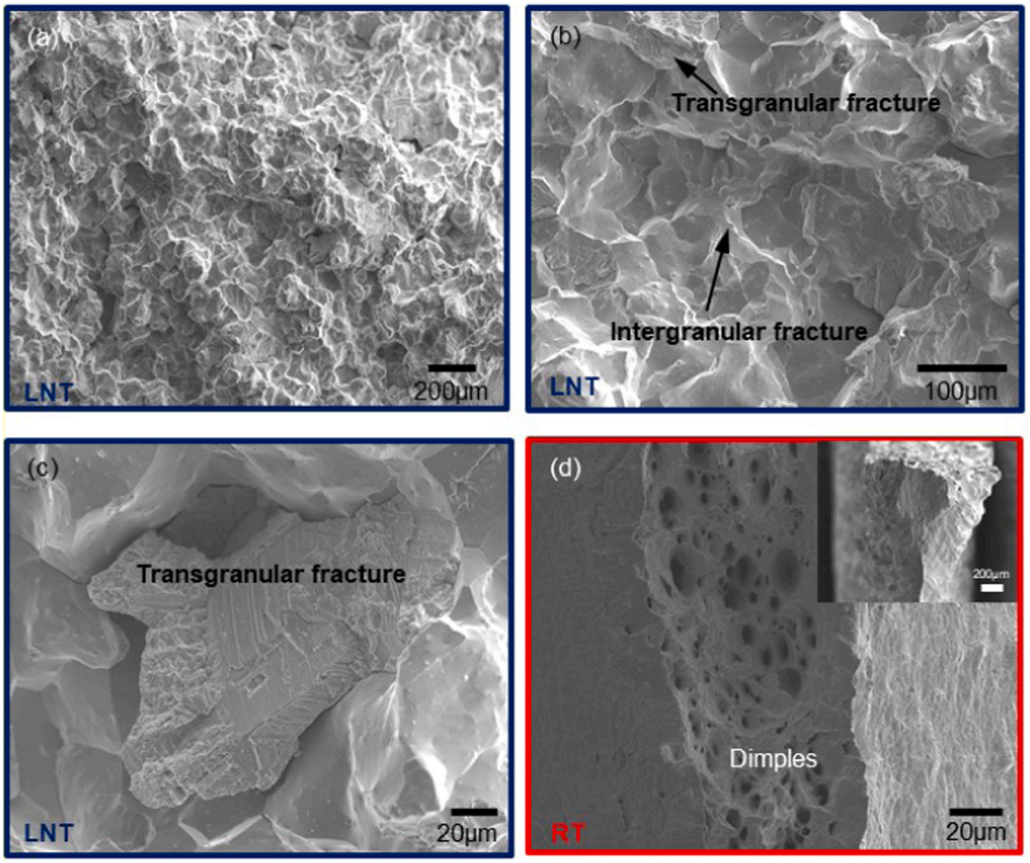

Fig. 2. SEM images of fractured Sn specimens at LNT and RT. (a) Overall fracture surface obtained at LNT. (b) Enlarged fracture morphology showing a hybrid fracture pattern with the most intergranular modes and some transgranular modes at LNT. (c) SEM images of one typical transgranular crack at LNT. (d) Ductile fracture surface with dimples at RT. Inset: the overall fracture morphology of Sn specimen at RT.

The fracture morphologies of tensile samples were examined using SEM (Zeiss, Merlin Compact). A TEM (FEI, Talos F200x) analysis was then carried out to characterize the structures of deformation twins generated in the cryogenic deformation of Sn. Thin Sn foils for TEM characterizations were prepared with focused ion beam (FIB, FEI, Helios Nanolab 600i) by cutting through the typical twin boundaries (TBs) that were determined from EBSD results.

3. Results

3.1. Mechanical behaviors at LNT and RT

Fig. 1a displays the engineering stress-strain curves obtained from uniaxial tensile tests at LNT and RT. As compared to those at RT, the yield strength, σ_y (0.2% engineering strain) increases from 10 MPa to 36 MPa (by ~260%) and the ultimate tensile strength, σ_{UTS} rises from 20 MPa to 78 MPa (by ~290%) at LNT. Despite this large increase in strength, the tensile ductility (engineering strain to failure, ε_f) declines markedly from 90% to 8%. It means that a DBT occurs in the polycrystalline Sn when the ambient temperature decreases to LNT, at which a premature fracture occurs during the strain hardening. Hence, the strain hardening behaviors are then investigated to reveal the deformation features accompanying with the transition and the DBT mechanism.

Here, to compare the strain hardening behaviors of polycrystalline Sn at different temperatures, the strain hardening rates ($d\sigma/d\varepsilon$) are normalized by the shear modulus G [25,26] (9 GPa at RT and 15 GPa at LNT [27,28]). Figs. 1b and 1c show the normalized strain hardening rate as a function of true strain (ε_t) and flow stress (σ-σ_y), respectively. In the LNT case, the strain hardening curve exhibits two distinguishable stages. The first stage features a continuous decrease (~G/5 to ~G/20) in strain hardening rates until a true strain of ~0.03 (inset of Fig. 1b) with a work hardening of ~25 MPa (Fig. 1c). The second stage is represented by a nearly constant hardening rate (i.e., linear hardening) of ~G/20 after straining beyond ~0.03. This linear hardening stage leads to a further increase of ~30 MPa in strength, but stops with an abrupt fracture at 0.07 true strain (Fig. 1b). This sudden stopping of linear hardening is particularly unusual. In FCC metals [29–31], linear hardening can be ascribed to the intersecting of deformation twins, but it is followed by a third stage in which hardening rates steadily decrease, commonly accompanying subsequent necking. Thus, this early termination of linear hardening strongly indicates that the BCT Sn, as a typical non-FCC metal, triggers an alternative mechanism behind deformation twinning. In the RT case, the normalized strain hardening rates fall into a monotonic decay, and approach zero (< G/100) at a true strain of only 0.05 (Fig. 1b). Even though the strain increases progressively, the hardening rates remain constant at around zero (± G/100) until a large strain of ~0.6. Afterward, the hardening rates become negative until the specimen ruptures at a true strain of ~0.65.

3.2. Tensile fracture morphologies at LNT and RT

Fractography offers clues to fracture initiation and propagation and thus helps reveal the transition of fracture modes with the decreasing temperature. Fig. 2 shows the tensile fracture morphologies obtained at LNT and RT. Overall fracture morphologies at LNT (Fig. 2a) exhibit distinctive characteristics of brittle fracture. The average size of the fracture facet is about 100 μm (Fig. 2b), which corresponds to the grain size of the as-prepared Sn samples (Fig. 3a),

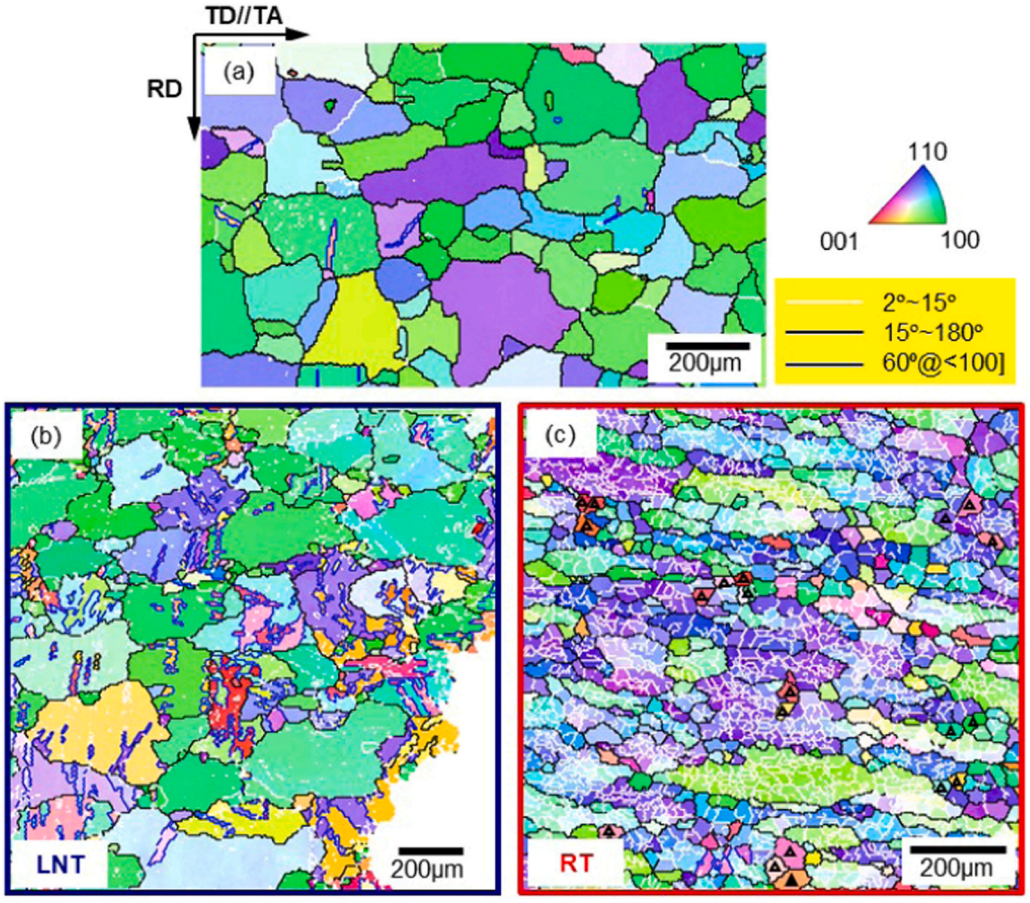

Fig. 3. ND-IPF of (a) as-cast Sn; fractured Sn specimens at (b) LNT and (c) RT. The corresponding color code for ND-IPF is used throughout the paper. Some DRXed grains in (c) are marked with triangles.

indicating that intergranular fractures occur mostly in the premature failure. Moreover, some transgranular fractures are occasionally observed on the fracture surface (Fig. 2c). On the other hand, Fig. 2d demonstrates that the Sn specimen exhibits a ductile fracture surface characterized by dimples after serve necking at RT. Hence, the fracture modes of polycrystalline Sn transform from ductile fracture with abundant dimples (Fig. 2d) to brittle intergranular fracture (Fig. 2a) with the temperature declining from RT to LNT.

3.3. Deformation microstructures at LNT and RT

The EBSD technique was used to analyze the surface close to the crack flanks of the fractured samples. Fig. 3 shows the inverse pole figures (IPF) for the crystal direction along the normal direction (ND) of the specimens. Here, high angle grain boundaries (HAGBs) with misorientations larger than 15° are traced by black lines, and low angle grain boundaries (LAGBs) with misorientations between 2° and 15° are outlined by white lines. In addition, the boundaries with a specific misorientation of 60° (± 5°) about < 100 > axis are defined with blue in all EBSD micrographs, because the {301} twins and {101} twins of Sn have the misorientations of 62.8°@ < 100 > and 57.2°@ < 100 > , respectively [7,32].

Before tensile loading, as-prepared (as-cast) Sn specimens have an equiaxial grain structure with an average grain size of 100 μm (Fig. 3a). Their misorientation angles exhibit a relatively homogeneous distribution without sharp peaks (Fig. 4a).

After the tensile fracture at LNT, most of the grains in the specimen are not elongated greatly, but the 60°@ < 100 > boundaries within individual grains account for 44.8% of all the boundaries (Table 1). In addition, the misorientations show a localized distribution with a peak fraction of 43% at around 63° (Fig. 4b), in agreement with the misorientation angle of 62.8° for {301} deformation twin in Sn [7,32]. Therefore, the above EBSD results suggest that the LNT tensile Sn specimens undergo significant {301} deformation twinning, which might be related to their considerable strain hardening (Fig. 1).

However, after the RT tensile failure, distinct sub-grain misorientations, which are described as intragranular graduated-colors in Fig. 3c, are found in the individual elongated grains of the specimens, indicating significant dislocation-mediated plasticity. Moreover, the LAGBs, which are typically located in the grain interiors, account for 59.2% (Table 1); and particularly, small misorientations (~4.45°) predominate (Fig. 4c). These results suggest that dynamic recovery (DRV) and dynamic recrystallization (DRX) accompany the plastic deformation. (DRXed grains are marked using triangles in Fig. 3c and the corresponding EBSD analysis can be seen in Supplementary Material 2). The DRV and DRX together with GB sliding (grain rotation)-governed deformation [33,34] lead to the long zero-hardening stage shown in Fig. 1b. However, deformation twinning is completely inhibited (only 0.3% 60°@ < 100 > boundaries), as listed in Table 1.

The above results about deformation microstructures reveal a transition in deformation mechanism of polycrystalline Sn from dislocation-mediated plasticity to deformation twinning-dominated with the decreasing temperature.

3.4. EBSD and TEM characterizations on the (301) deformation twin

On the surface of the LNT tensile Sn specimen, parallel lamellar **twins 2** bounded with the 60°@[010] boundaries are embedded

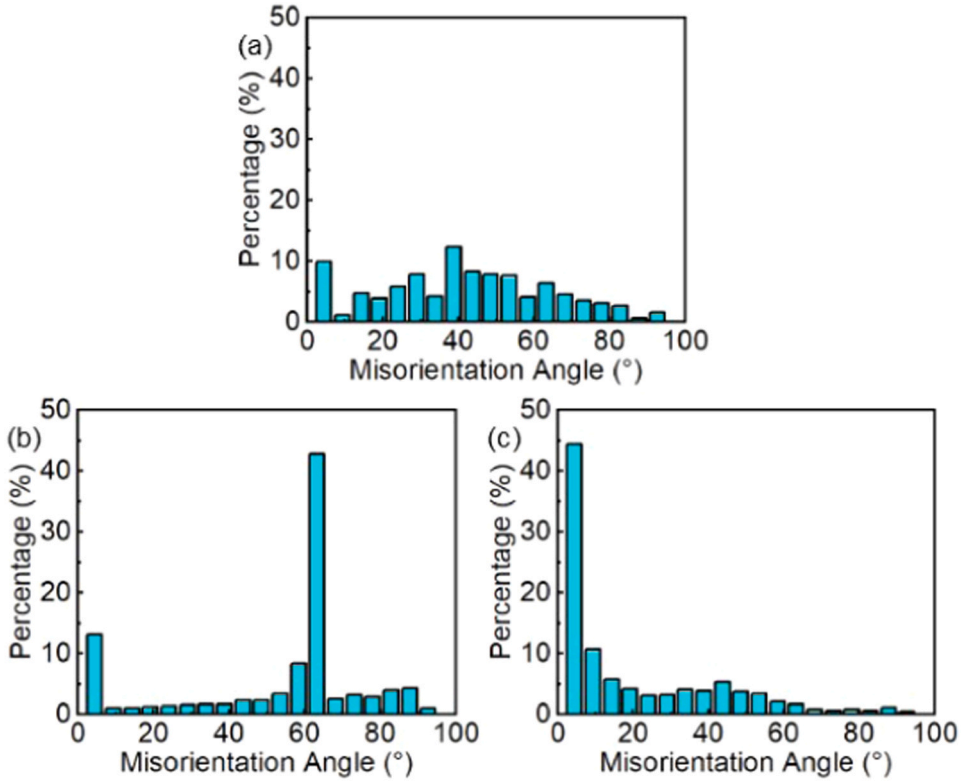

Fig. 4. Misorientation distributions of (a) as-cast Sn, (b) LNT tensile Sn, and (c) RT tensile Sn.

Table 1
The percentage of LAGBs, HAGBs and 60°@ < 100 > GBs in Fig. 3.

	LAGBs	HAGBs	60°@ < 100 > GBs
As-cast	6.7%	93.3%	4.2%
LNT(~77 K)	14.8%	85.2%	44.8%
RT(~293 K)	59.2%	40.8%	0.3%

within **matrix 1**, and there exists a (301) twin relationship between **parent 1** and **twin 2** according to the pole figure (Fig. 5a). (The detailed crystallography relationship between **parent 1** and **twin 2** can be seen in Supplementary Material 3). These (301) twins introduce a large number of TBs to divide the matrix, which can reduce the dislocation mean free path (dynamic Hall-Petch effects [35]). Therefore, these TBs can effectively prevent dislocation slip and serve as a stable hardening source.

TEM thin foils were cut on the (301) TB shown in Fig. 5a by FIB for further nano- and atomic-scale characterizations. The TEM and high-resolution TEM (HRTEM) images taken on the [010] zone axis indicate that the twin lies on the (301) plane (Fig. 5c-e). Three cells of **parent 1** and **twin 2** are superimposed on the HRTEM to show the atomic configurations of the (301) TB; they do not look symmetrical as the theoretical model shows [32]. For example, the arrangements of (10−1) planes appear asymmetrical (Fig. 5c). This asymmetry in atomic arrangements suggests the in-situ formation of edge dislocations along the (301) TB. The extra half-planes of atoms illustrated in the filtered inverse FFT image of the interfacial (10−1) diffraction spot (Fig. 5f) further confirm the formation of edge dislocations.

3.5. Intersecting twins

For FCC metals with low stacking fault energy, the intersecting of deformation twins leads to the linear hardening stage in their stress-strain responses at cryogenic temperatures [29–31]. Within the LNT tensile Sn specimens, a number of intersecting twins also appear, and a dense twin network is therefore developed. The twin network subdivides the original coarse grains and further reduce the dislocation mean free path, therefore more effectively blocking dislocation slip. As demonstrated in Fig. 6a, there are three primary twins (P_1, P_2, P_3) inside the matrix (M), all of which are confirmed to be {301} type twins but are different variants (Their mutual crystallography relations and determinations of twin variants can be seen in Supplementary Material 4). When these primary twins grow and encounter each other, P_2 and some P_1 cross P_3 while other P_1 are terminated at the boundaries of P_3 and P_2 or inside P_3. Such various intersecting relationships between twins generate considerable intersections within the original grain, at which a large number of dislocations are blocked. As a result, great local stress concentrations caused by dislocation accumulation occur around these intersections, as indicated by the high angles of kernel average misorientation (KAM) in Fig. 6c. In addition, when P_1 is terminated by P_2 and P_2 crosses P_3, secondary twins S_1 and S_2 are activated within P_1 and P_2, respectively (Fig. 6a-b, determinations of secondary twin variants can be seen in Supplementary Material 4). Secondary twins introduce new TBs and twin-twin intersections, at which the KAM values become higher (Fig. 6c). It suggests that higher stress concentrations occur at these new intersections because of the pile-up of a larger number of dislocations.

4. Discussions

4.1. Strain hardening mechanism before brittle fracture at LNT

According to Fig. 1, the brittle fracture at LNT occurs in the midst of strain hardening. In order to reveal the brittle fracture mechanisms, it is necessary to firstly elucidate the strain hardening mechanisms. Apart from higher hardening rates, the strain hardening curve at LNT has a remarkably different shape compared with that produced at RT (Fig. 1). In the RT case, after a rapid monotonic decay

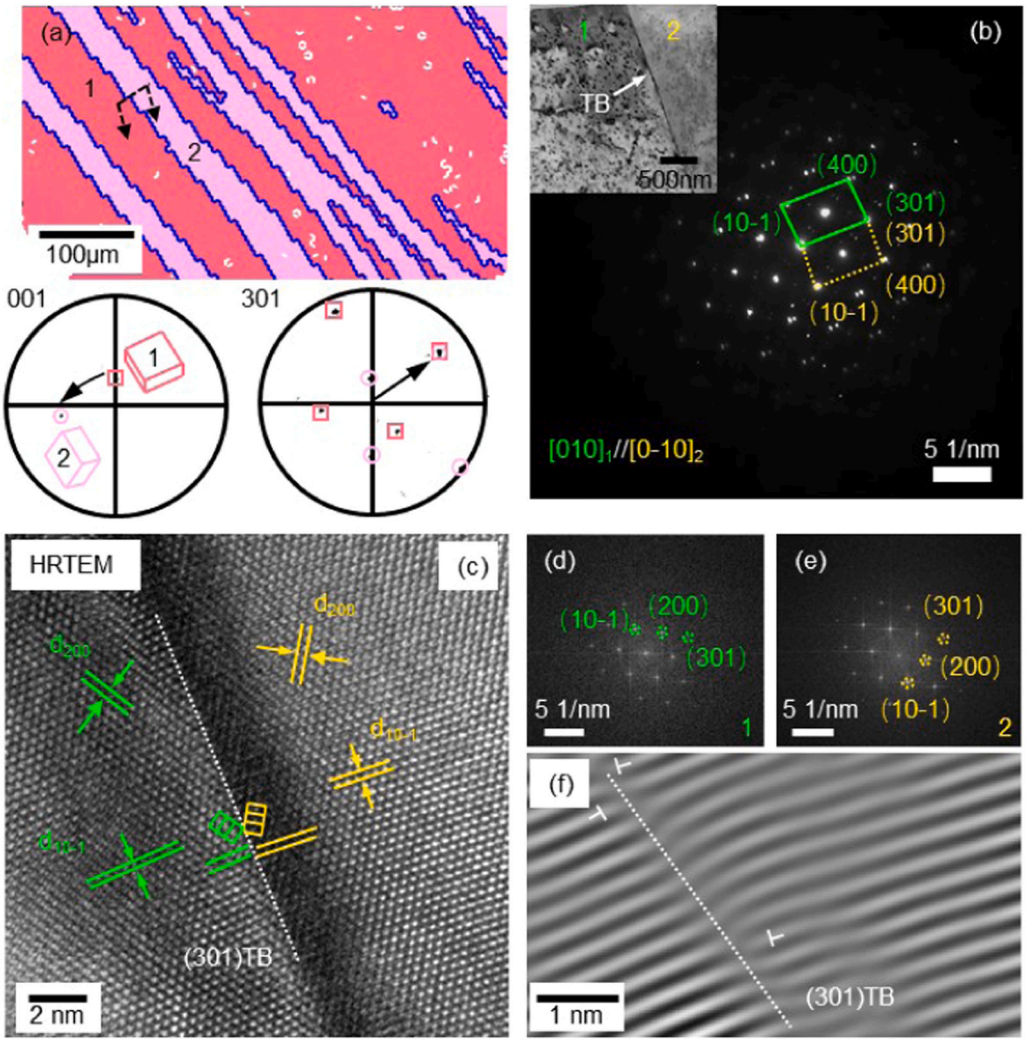

Fig. 5. (a) ND-IPF of lamella **twins 2** embedded within the **matrix 1** (black dashed arrows represent the FIB cutting position) with {001} and {301} pole figures. (b) Diffraction spots of **matrix 1** and **twin 2** with bright field TEM micrograph of the cut TEM foil displayed in the inset. (c) HRTEM image of the (301) twin with [010] zone axis. (d) and (e) demonstrate the FFT images of **matrix 1** and **twin 2**, respectively; (f) Filtered inverse FFT image of (10–1) plane along the (301) TB.

in normalized rates to zero at ~0.05 true strain, the hardening curve enters a fairly lengthy zero-hardening stage before fracture. In the LNT case, although the hardening rates also experience a monotonic decline at the beginning, there is a sharp downward inflection in the curve at ~0.015 true strain. Afterward, a hardening plateau with the normalized hardening rates of ~G/20 occurs at ~0.03 true strain. EBSD scans (Fig. 3b) after fracture suggest that substantial {301} deformation twins occur during the tensile deformation at LNT. Hence, the distinctive work hardening behaviors at this cryogenic temperature might be regulated by the different stages of deformation twinning.

Firstly, the sharp decrease in hardening rates at ~0.015 true strain is reminiscent of the downward inflection in hardening curves of Cu-3.1Sn, Cu-4.9Sn, Cu-30Zn (at%) and other low stacking fault energy FCC alloys due to the initiation of deformation twins [29–31]. These incipient twins tend to be parallel and occur on a given crystallographic plane, in which the interaction between slip and twinning is weak [29]. Namely, the formation of twins contributes only to an increment in the strain but not in the flow stress. Therefore, the sudden drop at the true strain of ~0.015 could be attributed to the bursting of {301} twins, while this onset strain for twinning appear insensitive to the strain rate [36,37]. Moreover, most of the {301} twin planes determined in Fig. 3b show a 60°~70° relationship with the tensile axis, confirming the clear tendency towards parallel twin planes at the beginning.

On the other hand, as proposed by a number of investigators [38–40], when deformation twins with non-parallel shear directions intersect at larger strains, a strong interaction has been observed between slip and twinning as well as between the blocked twins. In addition, intersecting twins can subdivide grains and further reduce the dislocation mean free path [29]. Consequently, flow stresses increase considerably, and the hardening rates are stabilized at a high level in the hardening rate-strain curves. Here, Fig. 1b demonstrates that the hardening rate-strain curve at LNT levels off after the initial decrease from G/5 to G/20, and the hardening rates remain nearly constant (linear hardening) at G/20 until Sn specimens rupture at a true strain of 0.07. Considering the above-mentioned hardening mechanisms that work with intersecting twins, the considerable intersecting {301} twins within individual grains (Fig. 6) contribute to stabilize the hardening rates. When these non-parallel {301} primary or secondary deformation twins intersect with each other, these generated twin-twin intersections further lead to the grain refinement and thus reduce the dislocation mean free path (dynamic Hall-Petch effects [35]). These intersections therefore act as more effective deformation barriers to dislocation glide and result in this linear hardening. As demonstrated in Fig. 6c,

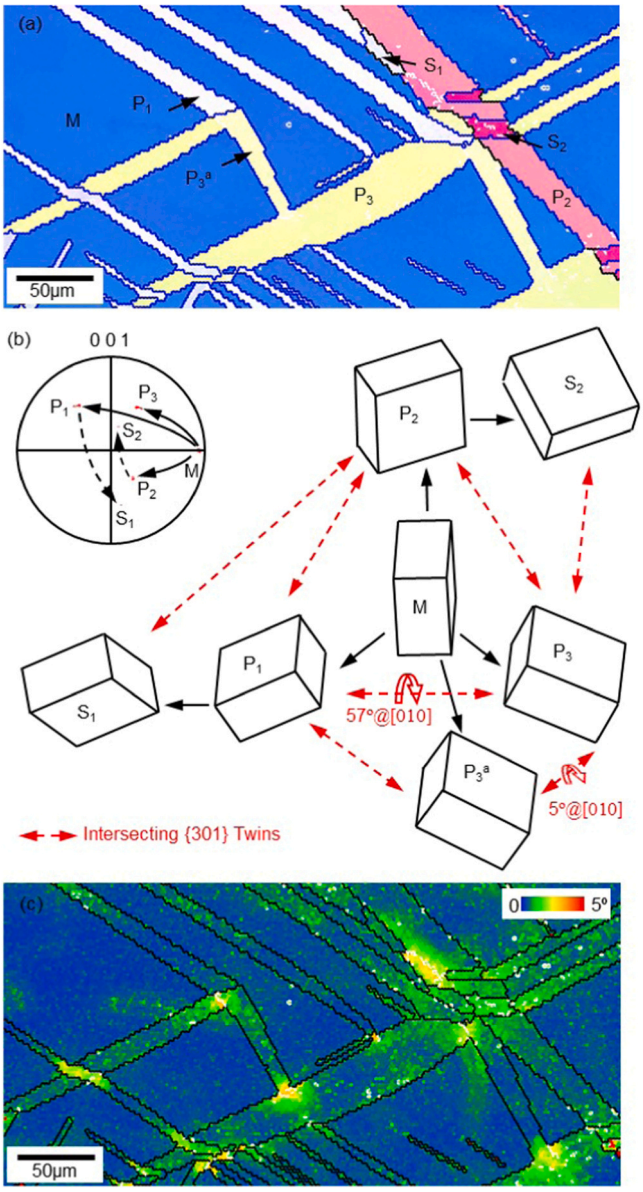

Fig. 6. (a) ND-IPF of the LNT tensile Sn specimens shows the primary twins (P) in the matrix (M) and secondary twins (S) developed within the primary twins. (b) 3D crystal orientation diagrams of matrix, primary twins and secondary twins in (a) with their mutual intersecting relationships (red dashed arrows). (c) Corresponding KAM map reveals local stress concentrations at these twin-twin intersections.

high KAM values at these generated twin-twin intersections (Fig. 6c) reveal that there exists a massive pile-up of dislocations.

4.2. Underlying mechanism of DBT occurring in polycrystalline Sn

When the temperature declines from RT to LNT, polycrystalline Sn specimens undergoes a transition from ductile fracture to brittle fracture (Figs. 1 and 2). Postmortem fractography (Fig. 2a-b) reveals that the brittle cracks at LNT propagate mainly in an intergranular mode. A detailed EBSD analysis of these microcracks along GBs (Fig. 7) reports an important fact that the cracked GBs intersect with the deformation twins (Fig. 7b-c). ***In-situ*** uniaxial tensile experiments at cryogenic temperatures [19] under optical microscope (**See** Supplementary Material 5 **and in-situ cryogenic tensile video**) further show that the brittle cracks initiate and propagate along the twin-GB intersections (Fig. S3). Furthermore, high stress concentrations around these twin-GB intersections are identified from the KAM map (Fig. 7d). It has been figured out that the presence of these local stress concentrations might plausibly be linked to the strong interaction between deformation twins and dislocations [41].

Supplementary material related to this article can be found online at doi:10.1016/j.jallcom.2022.163948.

Moreover, in body-centered cubic (BCC) metallic materials, it has been generally accepted that the interfacial high-stress field will induce GB fractures if it cannot be readily accommodated by continuous dislocation glide [42] when the deformation twins are rapidly arrested by some barrier twins or GBs. Accordingly, cracks are expected to appear immediately just after the nucleation of twins considering a huge gap between near-sonic twin elongation rate [43–46] and low dislocation velocity at cryogenic temperatures [47,48]. But in BCT Sn, the brittle fracture occurring is delayed by a marked plastic deformation after yielding, as shown in Fig. 1. This contradiction indicates an alternative mechanism triggers the brittle GB fracture in BCT Sn.

According to the **in - situ** tensile experiments at the cryogenic temperature, these cracks along the twin-GB intersections are found to occur after the thickening of the confined twins (Supplementary Material 5). Thus, the thickening of deformation twins might be responsible for the intergranular fracture. It is acknowledged that when these GB-blocked twins thicken, GBs are sheared by twin dislocations along the twinning direction (Fig. 8b) [49]. If these shear strains cannot be reconciled by the plastic deformation in neighboring grains, tensile stress concentrations will take place at these twin-GB intersections and increase with the accumulation of the shear strains as the twins thicken (Fig. 8c) [50,51]. Once the concentrated stress exceeds the strength of GB, the GB will be pulled open to nucleate a GB crack (Fig. 8d) [51]. Nucleation of the GB crack could be suppressed only by the compatible plastic deformation in neighboring grains through either deformation twinning or dislocation slip. Considering that the deformation twinning is grain orientation-dependent [52,53], the stress concentrations at these intersections should be relaxed mainly by dislocation slip. Accordingly, it can be reasoned that the twin-induced GB failure should be due to a velocity mismatch between dislocation slip and twin normal growth (twin thickening).

Here, we directly compare the twin-thickening rate and the slip velocity of dislocations at LNT. The average {301} twin thickness at LNT is calculated to be 50 μm from the EBSD scans (measurements were performed in at least 5 regions of 1×1 mm^2 of each specimen). Considering that {301} twins are activated at ~0.015 true strain (Fig. 1b) while the brittle fracture occurs after a true strain of ~0.07 (strain rate: 0.01/s), the average thickening rate of {301} twins can be estimated to be ~10 μm/s.

On the other hand, according to the Taylor hardening model [35], the increase in shear stress ($\Delta\tau$) due to dislocation interaction is given by:

$$\Delta\tau = \Delta\sigma/M = \alpha G b \rho^{1/2} \quad (1)$$

where $\Delta\sigma$ is the corresponding increase of the tensile stress, M is the Taylor Factor (0.99, See Supplementary Material 6), α is a constant (0.5 [35,53,54]), G is the shear modulus (15 GPa at 77 K), b is the magnitude of the Burgers vector (0.37 nm at 77 K [15,55]), and ρ is the dislocation density. Therefore, when the value of $\Delta\sigma$ is determined as σ-σ_y (8.3 MPa, Fig. 1c) where σ is the flow stress at the onset of deformation twinning and σ_y is the yield stress (the stress for the activation of deformation twinning decreases significantly with the increase of strain rate [42]), the value of ρ can be estimated as about 9×10^{12} m^{-2}. Furthermore, the plastic shear rate $\dot{\gamma}$ caused only by dislocation glide before the start of deformation twinning can be obtained according to the Orowan equation [56]:

$$\dot{\gamma} = M\dot{\varepsilon} = b\rho v_d \quad (2)$$

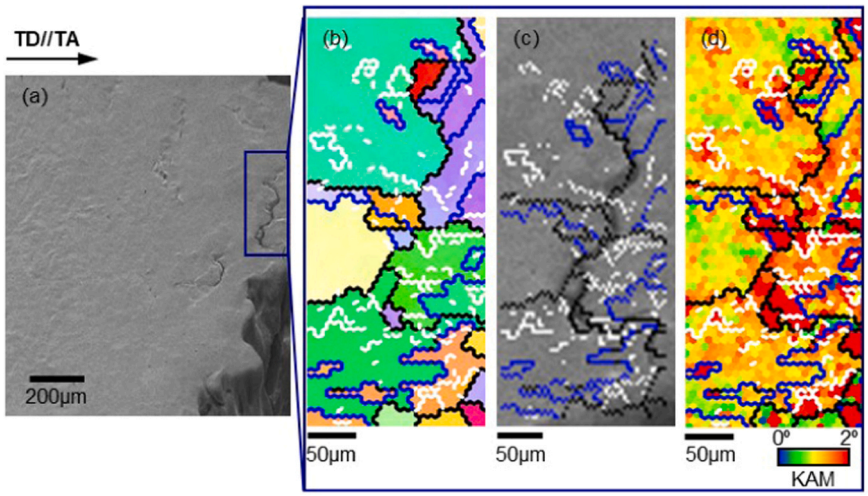

Fig. 7. (a) SEM micrograph displays the surface of fractured Sn specimen at LNT. (b) ND-IPF of the enclosed region by navy rectangle in (a). (c) Reproduced SEM image from (b) with only the boundaries retained shows that brittle cracks occur along the twin-GB intersections. (d) KAM map reveals local stress concentrations at these twin-GB intersections.

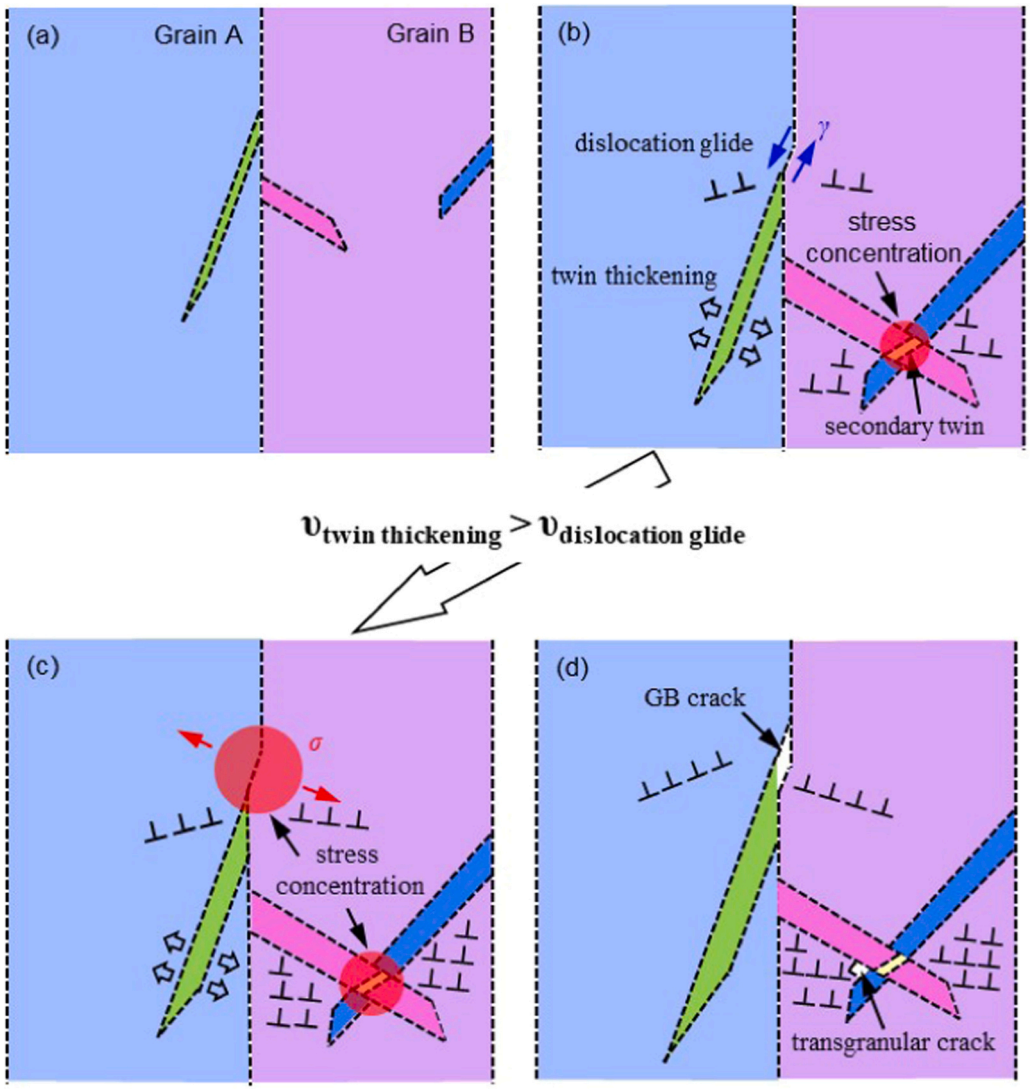

Fig. 8. Schematic diagrams illustrating the premature brittle fracture mechanisms at LNT. (a) Deformation twins nucleate from GBs. (b) The thickening of GB-blocked twins causes shear strains at the GB while intersecting of propagated primary twins and activated secondary twins leads to internal stress concentrations, both of which are required to be eliminated by dislocation glide. (c) Tensile stress concentrations occur at the twin-GB intersection due to the velocity gap between dislocation glide and twin thickening. (d) The GB crack and the transgranular crack occur.

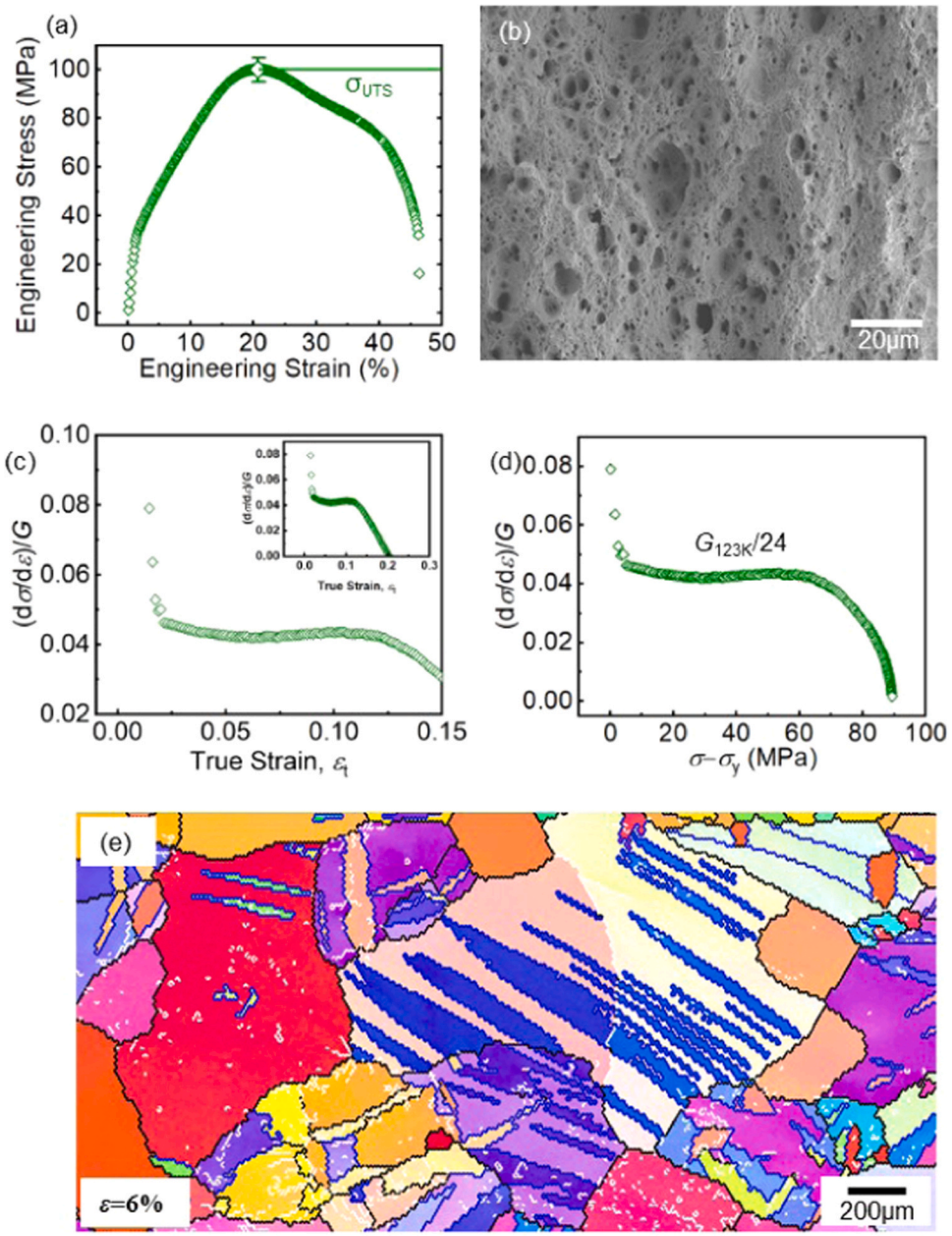

Fig. 9. Uniaxial tensile experimental results at 123 K. (a) Engineering stress-strain curve. (b) Fracture morphology. (c) Normalized strain hardening curve over a true strain to 0.15. Inset: the entire hardening curve until strain hardening rates become negative. (d) The plot of normalized strain hardening rates against flow stress, σ-σ_y. (e) ND-IPF of the Sn specimen after an engineering strain of 6%.

where M is the Taylor factor, $\dot{\varepsilon}$ is the tensile strain rate, b is the Burgers vector, and ρ is the dislocation density. Substituting these terms into Eq. 2, the slip velocity of dislocations in Sn at 77 K, v_d can be calculated to be ~3 μm/s; it is only 30% of the twin thickening rate (10 μm/s). In other words, while the confined {301} twins in BCT Sn are thickening, the stress concentrations at the twin-GB intersections could not be effectively relieved by dislocation glide due to this velocity gap. As a result, GB cracks occur at the intersections and then rapidly propagate in an intergranular mode.

With respect to the occasional transgranular cracks (Fig. 2c), this type of fractures usually adopts a preferred mode of cleavage on given planes. As suggested in Fig. 6c, when these non-parallel {301} twin planes intersect, the consequent intersections are stress concentration areas inside the grains (Fig. 8b-c). The concentrated stress could be relieved by dislocation slip [57], however, dislocations glide at such a slow velocity in BCT Sn (~3 μm/s) that the internal stress concentrations also cannot be eliminated promptly. Therefore, microcracks are likely to form at these twin-twin intersections too (Fig. 8d) and cleavage fractures occur on these {301} twin planes.

4.3. Verification of the DBT mechanism

In reality, {301} deformation twins in BCT Sn are commonly activated in deformation conditions at high strain rates and cryogenic temperatures [32]. It is noteworthy that deformation twinning is inherently athermal [58,59] while the dislocation slip velocity is sensitive to the temperature with a positive dependence. It indicates that the velocity gap proposed above only exists below a critical temperature, which exactly corresponds to the DBTT.

According to the empirical velocity law [45,60], the relationship of dislocation glide velocity with temperature is given by:

$$\upsilon_d = A\left(\frac{\tau}{\tau_0}\right)^m \exp\left(-\frac{Q}{kT}\right) \quad (3)$$

wherein the dislocation velocity υ_d depends on the temperature T (Kelvin), the resolved shear stress τ, the stress exponent m and the activation energy Q. The parameter A is a pre-exponential factor; τ_0 = 1 MPa to fix the unit of the stress. The value of Q is largely identical to that of self-diffusion in polycrystalline Sn (32 kJ/mol) [61–63]. According to Eq. 3, for example, the ratio of υ_d at 123 K to that at 77 K reaches approximately 500 (See Supplementary Material 7). Dislocations would glide at such a high velocity (~1500 μm/s) that shear strains at the GBs caused by the twin thickening (thickening rate: ~10 μm/s) could be readily accommodated at 123 K. Thus, it can be further deduced that the brittle fracture will not occur in polycrystalline Sn at 123 K.

To verify this deduction, the uniaxial tensile experiments were carried out at 123 K (± 1 K) under the same conditions. Instead of a premature brittle fracture, Sn specimens experience yielding, hardening, necking and final failure with ε_f of ~46% at 123 K (Fig. 9a). Compared to the LNT case (Fig. 1), the σ_y at 123 K decreases slightly to 32 MPa, but the σ_{UTS} increases dramatically to 100 MPa. Sn specimens exhibit a typical ductile fracture surface characterized by abundant dimples, as shown in Fig. 9b. At 123 K, the hardening curves of $(d\sigma/d\varepsilon)/G$ versus true strain, ε_t (Fig. 9c) and flow stress, σ-σ_y (Fig. 9d) display the slightly low hardening plateau of ~G/24. However, the hardening rates begin to decline gradually to zero after a complete hardening plateau at ~0.12 true strain. As a result, the work hardening is more considerable at 123 K (~89 MPa) than at LNT (~55 MPa), thereby leading to the ~28% increase in σ_{UTS}. Similarly, the linear hardening occurring at 123 K is also ascribed to the {301} deformation twins and their mutual intersection, as revealed in the ND-IPF EBSD scans of the Sn specimen after a 6% engineering strain at 123 K (Fig. 9e).

In conclusion, since the dislocation glide velocity is much higher than the twin thickening rate at 123 K and thus the velocity gap triggering the DBT does not exist, polycrystalline Sn specimens experience a complete hardening process and then ductile failure. It substantiates the proposed DBT mechanism that DBT will occur in polycrystalline BCT Sn when the dislocation slip velocity becomes smaller than the thickening rate of deformation twins with the decreasing temperature. Actually, the dominant mechanisms for the DBT of BCT Sn should still be the severe restrictions on dislocation glide at cryogenic temperatures, in line with the DBT mechanisms of BCC structures [64]. In addition to temperature, the deformation rate also influences the dislocation slip velocity while {301} deformation twins will also be activated in rapid deformation conditions. The findings we have presented above point to a critical need to reveal the effects of strain rate on the DBT mechanism. It also may offer new insights into the response of Sn-based solders to extreme working environments.

5. Conclusions

In this paper, we investigate the strain hardening behaviors of polycrystalline Sn before the cryogenic brittle fracture in uniaxial tensile tests and further propose the mechanism of DBT occurring with the declining temperature. The following conclusions can be drawn:

(1) Before the occurrence of brittle fracture at LNT (~77 K), considerable {301} deformation twins and intersecting twins are activated, and they contribute to the extremely high strain hardening plateau of ~G/20 in the stress-strain response. In contrast, continuous DRV and DRX cause a prolonged zero-hardening stage at RT (~293 K) where deformation twinning is completely suppressed. Moreover, an atomic configuration of the (301) deformation twin in BCT Sn has been obtained by HRTEM.
(2) It is found that the premature fracture occurring in the midst of the hardening plateau at LNT is due to the velocity mismatch between dislocation glide (~3 μm/s) and twin thickening (~10 μm/s). The large velocity difference renders the twin-thickening-induced shear strain at twin-GB intersections unable to be relaxed totally, leading to stress concentrations; under the concentrated stress, GB cracks ultimately nucleate at these intersections then rapidly propagate along the GBs.
(3) As the temperature declines, the plastic deformation mechanism of polycrystalline Sn gradually transforms from dislocation-mediated to deformation twinning-dominated. Due to the positive dependence of dislocation glide on temperature, the velocity gap between dislocation glide and twin thickening will appear below a critical temperature, triggering the DBT. In other words, the dominated DBT mechanisms should be the restriction on dislocation glide at cryogenic temperature. Accordingly, reducing the thickening rate of the deformation twins will be a potential strategy to design novel Sn-based solders with improved embrittlement resistance for cryogenic electronics.

CRediT authorship contribution statement

Xiaoliang Ji: Data curation, Formal analysis, Investigation, Methodology, Writing – original draft. **Rong An**: Formal analysis, Investigation, Supervision, Writing – review & editing. **Wei Zhou**: Conceptualization, Data curation, Methodology. **Ying Zhong**: Formal analysis, Writing – review & editing. **Fu Guo**: Data curation, Writing – review & editing. **Chunqing Wang**: Conceptualization, Funding acquisition, Supervision, Writing – review & editing.

Declaration of Competing Interest

The authors declare that they have no known competing financial interests or personal relationships that could have appeared to influence the work reported in this paper.

Acknowledgements

We greatly acknowledge the financial support of National Natural Science Foundation of China (No. U1537207). Great thanks to Engineers Shu Guo and Baoyou Zhang at Center of Analysis and Test, Harbin Institute of Technology, for FIB cutting, TEM and EBSD characterizations.

Appendix A. Supporting information

Supplementary data associated with this article can be found in the online version at doi:10.1016/j.jallcom.2022.163948.

References

[1] M. Abtew, G. Selvaduray, Lead-free solders in microelectronics, Mater. Sci. Eng. R 27 (2000) 95–141, https://doi.org/10.1016/S0927-796X(00)00010-3
[2] K.N. Tu, K. Zeng, Tin-lead (SnPb) solder reaction in flip chip technology, Mater. Sci. Eng. R 34 (2001) 1–58, https://doi.org/10.1016/S0927-796X(01)00029-8
[3] J.J. Stephens, D.R. Frear, Time-dependent deformation behavior of near-eutectic 60Sn-40Pb solder, Metall. Mater. Trans. 30A (1999) 1301–1313, https://doi.org/10.1007/s11661-999-0279-2
[4] K. Lambrinou, W. Maurissen, P. Limaye, B. Vandevelde, B. Verlinden, I.D. Wolf, A novel mechanism of embrittlement affecting the impact reliability of tin-based lead-free solder joints, J. Electron. Mater. 38 (2009) 1881–1895, https://doi.org/10.1007/s11664-009-0841-0
[5] P. Ratchev, B. Vandevelde, B. Verlinden, B. Allaert, D. Werkhoven, Brittle to ductile fracture transition in bulk Pb-free solders, IEEE Trans. Comp. Pack. Tech. 30 (2007) 416–423, https://doi.org/10.1109/TCAPT.2007.901744
[6] R.Y. Tian, Y.H. Tian, C.X. Wang, L.Y. Zhao, Mechanical properties and fracture mechanisms of Sn-3.0Ag-0.5Cu solder alloys and joints at cryogenic

temperatures, Mater. Sci. Eng. A 684 (2017) 697–705, https://doi.org/10.1016/j.msea.2016.12.058
[7] A. Lupinacci, J. Kacher, A. Eilenberg, A.A. Shapiro, P. Hosemann, A.M. Minor, Cryogenic in situ micro-compression testing of Sn, Acta Mater. 78 (2014) 56–64, https://doi.org/10.1016/j.actamat.2014.06.026
[8] P. Huybers, G. Denton, Antarctic temperature at orbital timescales controlled by local summer duration, Nat. Geosci. 1 (2008) 787–792, https://doi.org/10.1038/ngeo311
[9] NASA Solar System and Beyond, ⟨https://solarsystem.nasa.gov/planets/mars/in-depth/⟩ 2021, Accessed date: 1 December 2021.
[10] D. Palaferri, Y. Todorov, A. Bigioli, A. Mottaghizadeh, D. Gacemi, A. Calabrese, A. Vasanelli, L. Li, A.G. Davies, E.H. Linfield, F. Kapsalidis, M. Beck, J. Faist, C. Sirtori, Room temperature nine-μm-wavelength photodetectors and GHz-frequency heterodyne receivers, Nature 556 (2018) 85–94, https://doi.org/10.1038/nature25790
[11] M.S. Grinolds, S. Hong, P. Maletinsky, L. Luan, M.D. Lukin, R.L. Walsworth, A. Yacoby, Nanoscale magnetic imaging of a single electron spin under ambient conditions, Nat. Phys. 9 (2013) 215–219, https://doi.org/10.1038/nphys2543
[12] K.M. Yip, N. Fischer, E. Paknia, A. Chari, H. Stark, Atomic-resolution protein structure determination by cryo-EM, Nature 587 (2020) 157–161, https://doi.org/10.1038/s41586-020-2833-4
[13] X.L. Ji, R. An, F. Ma, J.W. Hu, C.Q. Wang, Unique buoyancy-force-based kinetics determination of beta to alpha phase transformation in bulk tin plates, Mater. Des. 190 (2020) 108550, https://doi.org/10.1016/j.matdes.2020.108550
[14] B. Cornelius, S. Treivish, Y. Rosenthal, M. Pecht, The phenomenon of tin pest: a review, Microelectron. Reliab. 79 (2017) 175–192, https://doi.org/10.1016/j.microrel.2017.10.030
[15] M. Nagasaka, Temperature dependence of plastic deformation in white tin crystals, Jpn. J. Appl. Phys. 28 (1989) 446–452, https://doi.org/10.1143/JJAP.28.446
[16] B. Gludovatz, A. Hohenwarter, K.V.S. Thurston, H. Bei, Z. Wu, E.P. George, R.O. Ritchie, Exceptional damage-tolerance of a medium-entropy alloy CrCoNi at cryogenic temperatures, Nat. Commun. 7 (10602) (2016) 1–8, https://doi.org/10.1038/ncomms10602
[17] Z. Wu, C.M. Parish, H. Bei, Nano-twin mediated plasticity in carbon-containing FeNiCoCrMn high entropy alloys, J. Alloy. Compd. 647 (2015) 815–822, https://doi.org/10.1016/j.jallcom.2015.05.224
[18] N.D. Stepanov, D.G. Shaysultanov, R.S. Chernichenko, N. Yu Yurchenko, S.V. Zherebtsov, M.A. Tikhonovsky, G.A. Salishchev, Effect of thermomechanical processing on microstructure and mechanical properties of the carbon-containing CoCrFeNiMn high entropy alloy, J. Alloy. Compd. 693 (2017) 394–405, https://doi.org/10.1016/j.jallcom.2016.09.208
[19] X.L. Ji, Q. An, Y.P. Xia, R. An, R. Zheng, C.Q. Wang, Maximum shear stress-controlled uniaxial tensile deformation and fracture mechanisms and constitutive relations of Sn–Pb eutectic alloy at cryogenic temperatures, Mater. Sci. Eng. A 819 (2021) 141523, https://doi.org/10.1016/j.msea.2021.141523
[20] Y. Ding, C.Q. Wang, Y.H. Tian, M.Y. Li, Influence of aging treatment on deformation behavior of 96.5Sn3.5Ag lead-free solder alloy during in situ tensile tests, J. Alloy. Compd. 428 (2007) 274–285, https://doi.org/10.1016/j.jallcom.2006.02.069
[21] Q. An, R. An, C.Q. Wang, H. Wang, Ductile-to-brittle transition in fracture behaviors of common solder alloys over a temperature range down to −150 ºC, Mater. Today Commun. 29 (2021) 102962, https://doi.org/10.1016/j.mtcomm.2021.102962
[22] K.N. Prabhu, P. Deshapande, Satyanarayan, Effect of cooling rate during solidification of Sn–9Zn lead-free solder alloy on its microstructure, tensile strength and ductile–brittle transition temperature, Mater. Sci. Eng. A 533 (2012) 64–70, https://doi.org/10.1016/j.msea.2011.11.035
[23] P. Limaye, W. Maurissen, K. Lambrinou, F. Duflos, B. Vandevelde, B. Allaert, J. Hillaert, D. Vandepitte, B. Verlinden, Low-temperature embrittlement of lead-free solders in joint level impact testing, in: 2009 9th Electronics Packaging Technology Conference, IEEE, 140–151. https://doi.org/10.1109/EPTC.2007.4469705.
[24] Y.H. Zhang, W.Z. Han, Mechanism of brittle-to-ductile transition in tungsten under small-punch testing, Acta Mater. 220 (2021) 117332, https://doi.org/10.1016/j.actamat.2021.117332
[25] E.P. George, W.A. Curtin, C.C. Tasan, High entropy alloys: a focused review of mechanical properties and deformation mechanisms, Acta Mater. 188 (2020) 435–474, https://doi.org/10.1016/j.actamat.2019.12.015
[26] S.-H. Joo, H. Kato, M.J. Jang, J. Moon, C.W. Tsai, J.W. Yeh, H.S. Kim, Tensile deformation behavior and deformation twinning of an equimolar CoCrFeMnNi high-entropy alloy, Mater. Sci. Eng. A 689 (2017) 122–133, https://doi.org/10.1016/j.msea.2017.02.043
[27] Matweb, Material Propertie Data-Tin (Sn) ⟨http://www.matweb.com/search/DataSheet.aspx?MatGUID=64d7cf04332e428dbca9f755f4624a6c&ckck=1⟩ Accessed data: 1 December 2021.
[28] A.U. Telang, T.R. Bieler, A. Zamiri, F. Pourboghrat, Incremental recrystallization/grain growth driven by elastic strain energy release in a thermomechanically fatigued lead-free solder joint, Acta Mater. 55 (2007) 2265–2277, https://doi.org/10.1016/j.actamat.2006.11.023
[29] S. Krishnamurthy, R.E. Reed-Hill, Concerning the role of mechanical twinning on the stress-strain behavior Cu-4.9 At. Pct Sn Alloy, Metall. Trans. A 11A (1980) 565–572, https://doi.org/10.1007/BF02648534
[30] S. Asgari, E. El-Danaf, S.R. Kalidindi, R.D. Doherty, Strain hardening regimes and microstructural evolution during large strain compression of low stacking fault energy fcc alloys that form deformation twins, Metall. Mater. Trans. A 28A (1997) 1781–1795, https://doi.org/10.1007/s11661-997-0109-3
[31] S. Krishnamurthy, K.W. Qian, R.E. Reed-Hill, Effects of deformation twinning on the stress-strain curves of low stacking fault energy face-centered cubic alloys, in: J. Steele, J. McCall (Eds.), Practical Application of Quantitative Metallography, ASTM International West Conshohocken, 1984, pp. 41–64.
[32] T.K. Lee, T.R. Bieler, C.U. Kim, H. Ma, Fundamentals of Lead-Free Solder Interconnect Technology: From Microstructures to Reliability, Springer, New York, 2015.
[33] J. Han, J. Sun, T.Y. Wen, F. Guo, Analysis of continuous recrystallization (sub)grain rotation behavior in Pb-free solder bumps under a 0.1 μm/s shear rate, J. Mater. Sci. Mater. Electron. 29 (2018) 10992–10999, https://doi.org/10.1007/s10854-018-9181-2
[34] C.Y. Cai, J.F. Xu, H.Y. Wang, S.B. Park, A comparative study of thermal fatigue life of eutectic Sn-Bi, hybrid Sn-Bi/SAC and SAC solder alloy BGAs, Microelectron. Reliab. 119 (2021) 114065, https://doi.org/10.1016/j.microrel.2021.114065
[35] G. Laplanche, A. Kostka, O.M. Horst, G. Eggeler, E.P. George, Microstructure evolution and critical stress for twinning in the CrMnFeCoNi high-entropy alloy, Acta Mater. 118 (2016) 152–163, https://doi.org/10.1016/j.actamat.2016.07.038
[36] G. Bajargan, G. Singh, D. Sivakumar, U. Ramamurty, Effect of temperature and strain rate on the deformation behavior and microstructure of a homogenized AZ31 magnesium alloy, Mater. Sci. Eng. A 579 (2013) 26–34, https://doi.org/10.1016/j.msea.2013.04.088
[37] X. Yu, Y.L. Li, Q.M. Wei, Y.Z. Guo, T. Suo, F. Zhao, Microstructure and mechanical behavior of ECAP processed AZ31B over a wide range of loading rates under compression and tension, Mech. Mater. 86 (2015) 55–70, https://doi.org/10.1016/j.mechmat.2015.03.001
[38] S. Mahajan, G.Y. Chin, Formation of deformation twins in f.c.c. crystals, Acta Metall. 21 (1973) 173–179, https://doi.org/10.1016/0001-6160(73)90085-0
[39] S. Mahajan, G.Y. Chin, The interaction of twins with existing substructure and twins in cobalt-iron alloys, Acta Metall. 22 (1974) 1113–1119, https://doi.org/10.1016/0001-6160(74)90066-2
[40] L. Remy, Twin-slip interaction in f.c.c. crystals, Acta Metall. 25 (1977) 711–714, https://doi.org/10.1016/0001-6160(77)90013-X
[41] S. Mahajan, D.F. Williams, Deformation twinning in metals and alloys, Int. Metall. Rev. 18 (1973) 43–61, https://doi.org/10.1179/imtlr.1973.18.2.43
[42] J.W. Christian, S. Mahajan, Deformation twinning, Prog. Mater. Sci. 39 (1995) 1–157, https://doi.org/10.1016/0079-6425(94)00007-7
[43] S.V. Lubenets, V.I. Startsev, L.S. Fomen, Dynamics of twinning in metals and alloys, Phys. Stat. Sol. A 92 (1985) 11–55, https://doi.org/10.1002/pssa.2210920102
[44] B. Chalmers, The cry of tin, Nature 30 (1932) 650–651, https://doi.org/10.1038/129650a0
[45] J.H. Brunton, M.P.W. Wilson, The kinetics of twinning in zinc and tin crystals, Proc. R. Soc. Lond. A, 309 (1969) 345–361. ⟨https://doi.org/10.1098/rspa.1969.0046⟩.
[46] D.F. Williams, C.N. Reid, A dynamic study of twin-induced brittle fracture, Acta Metall. 19 (1971) 931–937, https://doi.org/10.1016/0001-6160(71)90086-1
[47] A.P.L. Turner, T.V. JR, The effect of stress and temperature on the velocity of dislocations in iron monocrystals, Acta Metall. 18 (1970) 1225–1235, https://doi.org/10.1016/0001-6160(70)90113-6
[48] M. Tanaka, E. Tarleton, S.G. Roberts, The brittle–ductile transition in single-crystal iron, Acta Mater. 56 (2008) 5123–5129, https://doi.org/10.1016/j.actamat.2008.06.025
[49] Z.D. Kou, Y.Q. Yang, L.X. Yang, B. Huang, X. Luo, Twinning-assisted void initiation and crack evolution in Cu thin film: An in situ TEM and molecular dynamics study, Mater. Sci. Eng. A 737 (2018) 336–340, https://doi.org/10.1016/j.msea.2018.09.069
[50] Y.F. Zhang, P.C. Millett, M. Tonks, B. Biner, Deformation-twin-induced grain boundary failure, Scr. Mater. 66 (2012) 117–120, https://doi.org/10.1016/j.scriptamat.2011.10.021
[51] Y.F. Zhang, P.C. Millett, M. Tonks, S.B. Biner, Deformation twins in nanocrystalline body-centered cubic Mo as predicted by molecular dynamics simulations, Acta Mater. 60 (2012) 6421–6428, https://doi.org/10.1016/j.actamat.2012.08.029
[52] P. Yang, Q. Xie, L. Meng, H. Ding, Z. Tang, Dependence of deformation twinning on grain orientation in a high manganese steel, Scr. Mater. 55 (2006) 629–631, https://doi.org/10.1016/j.scriptamat.2006.06.004
[53] Z.W. Huang, S.B. Jin, H. Zhou, Y. Li, Y. Cao, Y.T. Zhu, Evolution of twinning systems and variants during sequential twinning in cryo-rolled titanium, Int. J. Plast. 112 (2019) 52–67, https://doi.org/10.1016/j.ijplas.2018.08.008
[54] J.E. Bailey, The dislocation density, flow stress and stored energy in deformed polycrystalline copper, Philos. Mag. 8 (1963) 223, https://doi.org/10.1080/14786436308211120
[55] M.A. Bhatia, I. Adlakha, G. Lu, K.N. Solanki, Generalized stacking fault energies and slip in β-tin, Scr. Mater. 123 (2016) 21–25, https://doi.org/10.1016/j.scriptamat.2016.05.038
[56] C. Zambaldi, D. Raabe, Plastic anisotropy of γ-TiAl revealed by axisymmetric indentation, Acta Mater. 58 (2010) 3516–3530, https://doi.org/10.1016/j.actamat.2010.02.025
[57] P. Müllner, C. Solenthaler, P.J. Uggowitzer, M.O. Speidel, Brittle fracture in austenitic steel, Acta Metall. Mater. 42 (1994) 2211–2217, https://doi.org/10.1016/0956-7151(94)90300-X
[58] S. Zhao, R. Zhang, Y. Chong, X. Li, A. Abu-Odeh, E. Rothchild, D.C. Chrzan, M. Asta, J.W. Morris, A.M. Minor, Defect reconfiguration in a Ti–Al alloy via electroplasticity, Nat. Mater. (2020), https://doi.org/10.1038/s41563-020-00817-z

[59] M.A. Meyers, O. Vohringer, V.A. Lubarda, The onset of twinning in metals: a constitutive description, Acta Mater. 49 (2001) 4025–4039, https://doi.org/10.1016/S1359-6454(01)00300-7
[60] A. Hartmaier, P. Gumbsch, Scaling relations for crack-tip plasticity, Philos. Mag. A 82 (2002) 3187–3200, https://doi.org/10.1080/01418610208240432
[61] S. Maruyama, Dynamic behavior of twinning in tin crystals at various temperatures and strain rates, J. Phys. Soc. Jpn. 15 (1960) 1243–1261, https://doi.org/10.1143/JPSJ.15.1243
[62] F.Q. Yang, J.C.M. Li, Deformation behavior of tin and some tin alloys, J. Mater. Sci. Mater. Electron 18 (2007) 191–210, https://doi.org/10.1007/978-0-387-48433-4_12
[63] C.Y. Cai, J.F. Xu, H.Y. Wang, S.B. Park, Reliability of homogeneous Sn-Bi and hybrid Sn-Bi/SAC BGAs, in: 70th IEEE Electronic Components and Technology Conference, 2020, pp. 1496–1501.
[64] J.W. Morris Jr, Stronger, tougher steels, Science 320 (2008) 1022–1023, https://doi.org/10.1126/science.1158994